ACS APPLIED MATERIALS & INTERFACES

www.acsami.org Research Article

Modulated Sn Oxidation States over a Cu_2O-Derived Substrate for Selective Electrochemical CO_2 Reduction

Mengran Li,*,⊥ Xiaohe Tian,⊥ Sahil Garg, Thomas E. Rufford,* Peiyao Zhao, Yuming Wu, Anya Josefa Yago, Lei Ge, Victor Rudolph, and Geoff Wang

Cite This: *ACS Appl. Mater. Interfaces* 2020, 12, 22760−22770 Read Online

ACCESS | Metrics & More | Article Recommendations | Supporting Information

ABSTRACT: Pursuing high catalytic selectivity is challenging but paramount for an efficient and low-cost CO_2 electrochemical reduction (CO_2R). In this work, we demonstrate a significant correlation between the selectivity of CO_2R to formate and the duration of tin (Sn) electrodeposition over a cuprous oxide (Cu_2O)-derived substrate. A Sn electrodeposition time of 120 s led to a cathode with a formate Faradaic efficiency of around 81% at −1.1 V vs reversible hydrogen electrode (RHE), which was more than 37% higher than those of the Sn foil and the sample treated for 684 s. This result highlights the significant role of the interface between deposited Sn and the cuprous-derived substrate in determining the selectivity of CO_2R. High-resolution X-ray photoelectron spectra revealed that the residual cuprous species at the Cu/Sn interfaces could stabilize Sn species in oxidation states of 2+ and 4+, a mixture of which is essential for a selective formate conversion. Such modulation effects likely arise from the moderate electronegativity of the cuprous species that is lower than that of Sn^{2+} but higher than that of Sn^{4+}. Our work highlights the significant role of the substrate in the selectivity of the deposited catalyst and provides a new avenue to advance selective electrodes for CO_2 electrochemical reduction.

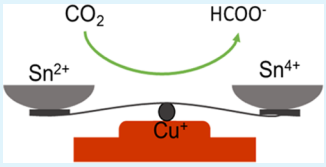

KEYWORDS: *CO_2 electrochemical reduction, formate production, electronegativity, tin electrocatalyst, catalyst substrate*

■ INTRODUCTION

The electrochemical CO_2 reduction (CO_2R) holds promise to mitigate CO_2 emissions due to its unparalleled advantages such as mild operating conditions, modulable design, and capability to integrate the existing carbon-intensive industrial processes with renewable energy from wind and solar.[1−3] This process can convert CO_2 into various valuable products such as CO, $HCOO^-$/HCOOH, CH_4, C_2H_4, and alcohols.[4−6] Notably, the production of HCOOH from CO_2 appears economically feasible because of its low energy demand and relatively high commercial value.[7] However, a low product selectivity of CO_2R lowers the energy efficiency and increases the complexity of downstream product separation, which consequently leads to a costly overall CO_2R process. Therefore, pursuing catalysts that activate selective CO_2R is imperative to increase the viability of this technology.

Tin (Sn)-based materials are promising catalysts for CO_2R to produce formate because of their low material cost, low toxicity, and the relatively high selectivity toward formate.[8−11] Most of the works,[12,13] including our recent work,[14] reported a strong dependency of formate selectivity on the oxidation state of Sn. This trend is supported by Baruch et al.,[15] who used in situ infrared spectroscopy measurements to reveal that the CO_2R over the Sn metal surface likely proceeds via a surface-bound carbonate (*OCHO intermediate) interacting with Sn(II) oxyhydroxide species. Dutta et al. also observed a strong correlation between the oxidation states of tin oxide nanoparticles and Faradaic efficiency (FE) to formate via time- and potential- resolved in situ Raman characterization.[16] Through combined density functional theory calculations and experimental investigations, An et al.[17] unveiled that the Sn^{4+} reduces overpotentials, Sn^{2+} promotes formate production, and oxide/metal interfaces suppress unwanted hydrogen evolution reaction (HER).

Many strategies have been proposed to enhance the formate selectivity of Sn-based catalysts, including introducing heterogeneous atoms and optimizing particle size and morphologies.[10,18−22] For example, Zheng et al.[19,23] demonstrated an excellent formate selectivity up to 93−95% over a slightly oxidized Sn, as imparted by Cu or sulfur. Liang et al.[24] reported an ultrasmall SnO_2 that achieved a peak Faradaic efficiency of formate of 74% at −0.73 V vs a reversible hydrogen electrode (RHE). In addition to chalcogenide[23,25] and oxide derivation,[10,12] another effective strategy to control the oxidation state of transition metals is to control the electronegativity difference between active metal sites and their neighboring dopants. This strategy has been well exemplified by our previous work at UQ to develop metal oxide-based electrode catalysts for fuel cell applications.[26−28] Note that Cu^+

Received: January 8, 2020
Accepted: April 27, 2020
Published: April 27, 2020

Downloaded via NEWCASTLE UNIV on July 13, 2020 at 08:39:35 (UTC).
See https://pubs.acs.org/sharingguidelines for options on how to legitimately share published articles.

ACS Publications © 2020 American Chemical Society

https://dx.doi.org/10.1021/acsami.0c00412
ACS Appl. Mater. Interfaces 2020, 12, 22760−22770

has an electronegativity of 1.56 that falls in between 1.73 for Sn^{4+} and 1.34 for Sn^{2+}.[29] Mistry et al.[30] reported that the cuprous species exist on oxide-derived copper surfaces during CO_2R. Under CO_2R potentials, this electronegativity difference could allow Cu^+ to stabilize the oxidation states of Sn because the presence of Cu^+ (electronegativity of 1.56) can donate electrons to Sn^{4+} at an electronegativity of 1.73 but Cu^+ can accept electrons from Sn^{2+} at 1.34.[29]

In this work, we oxidized Cu foils to produce a Cu_2O layer on the foils and then used chronopotentiometric electrodeposition to deposit the Sn catalyst on the Cu_2O-derived layer. We observed a strong correlation between the electrodeposition time, which increased the Sn coverage over the Cu_2O-derived substrate and affected the area of the Sn/Cu interfaces and the selectivity of the cathode for CO_2R to formate. Our analysis of the surface composition, oxidation states, and morphology of the Sn/Cu_2O-derived electrodes revealed that the deposition time and consequently the Sn/Cu_2O-derived interfaces affect the oxidation state of Sn atoms on the surface and therefore the catalyst's selectivity for CO_2R to formate. This modulation effect likely arises from the electronegativity of Cu^+ that is lower than that of Sn^{4+} but higher than that of Sn^{2+}[29] and balances the exposure of Sn^{2+}/Sn^{4+} on the surface. This work demonstrated that an optimal catalyst deposition time exists to achieve a selective CO_2R and highlighted the essential role of catalyst substrate in determining the selectivity of the catalysts.

■ EXPERIMENTAL SECTION

Material Preparation. Copper foils (0.5 mm, ≥99.99%, Sigma-Aldrich) were polished with the diamond polishing solution (ALS, Japan) to a mirror finish, then rinsed with deionized water and ethanol, and sonicated for 15 min in 0.5 M H_2SO_4 and then in deionized water. We refer to the polished foil as fresh Cu. The surface of the fresh Cu foils was oxidized to a layer of Cu_2O by immersing the Cu foil in a stirred chemical bath of 0.668 M Na_2SnO_3 (95%, Sigma-Aldrich) and 0.375 M NaOH (≥98%, Sigma-Aldrich) at 55 °C for 30 min. Then, we electrodeposited Sn onto the oxidized Cu surface from the Na_2SnO_3 + NaOH solution at an applied current density of 72 mA cm^{-2} using a Pt foil counter electrode and AglAgCl (3 M NaCl) (from ALS Japan) reference electrode. We controlled the electrodeposition time to be 20, 30, 60, 120, 240, and 684 s and kept a sample that was soaked only in the solution without any current applied (i.e., the sample label 0 s). As a benchmark for CO_2R measurements, we also prepared a polished Sn foil (0.5 mm 99.998% from Sigma-Aldrich) cathode using the same polishing procedure described for the Cu foils. The area of the electrode was around 1.5−2.5 cm^2, and the exact area of each electrode was recorded.

Electrochemical Measurements. We performed the CO_2R experiments using a three-electrode configuration in an H-type electrochemical cell with a Nafion 117 separator (from FuelCellStore) in similar procedures to what we have described elsewhere.[31] The working electrode (e.g., fresh Cu, 0 s sample, Sn on Cu_2O, or Sn foil) was sonicated in deionized water for 2 min and then immediately immersed in 70 mL of 0.5 M $KHCO_3$ solutions in the cathode chamber of the H-cell with an AglAgCl (3 M NaCl) reference electrode. A 0.6 cm diameter graphite rod (Sigma-Aldrich) was used as the counter electrode in 30 mL of 0.5 M $KHCO_3$ in the anode chamber. The cell was prepared for CO_2R experiments by first purging the electrolytes with Ar and then purging the catholyte with CO_2 (99.999%, Supagas, Australia) for at least 30 min.

All CO_2R tests were performed at room temperature and ambient pressure and controlled by a Metrohm Autolab PGSTAT302N potentiostat. The pH and temperature of the catholyte were measured continuously with a Metrohm LL Unitrode PT1000 probe. During CO_2R experiments, CO_2 was continuously bubbled through the catholyte at 30 sccm using a mass flow controller (MKS Instruments, ±1% resolution). The catholyte and anolyte were each continuously stirred at 500 rpm. Electrode potentials were converted into potentials vs reversible hydrogen electrode (RHE) by using

$$E_{RHE} = E_{AglAgCl} + \frac{2.303RT}{F}pH + 0.195 \quad (1)$$

where $E_{AglAgCl}$ is the measured potential vs AglAgCl RE, R is the universal gas constant, T is the measurement temperature in K, the pH of the catholyte was measured by an LL Unitrode Pt1000 probe, and F is the Faraday constant (96 485 C·mol^{-1}).

The overpotential η can be calculated using

$$\eta = E_{RHE} - E_{eq} \quad (2)$$

where E_{eq} is the thermodynamic equilibrium potential, and its value is −0.42 at T = 298 K and pH = 7.45. A detailed calculation can be found in the Supporting Information (SI).

Product Analyses. Gas products from CO_2R were analyzed using a Shimadzu GC-2030 gas chromatograph with a ShinCarbon packed column (ST 80/100, 2 mm ID, 1/8 OD Silco, Restek), a thermal conductivity detector (TCD), and a flame ionization detector (FID). Argon (Ar, 99.999%, Supagas Australia) and hydrogen (H_2, 99.999% BOC Australia) were used as the carrier gas for the TCD and FID, respectively, with zero air as the balance gas for the FID. The gas chromatography (GC) was calibrated daily using a standard calibration gas consisting of 10% H_2 and 10% CO balanced with Ar. The FE_i of gas product species i—CO and H_2 were the only major CO_2R gas products detected in these experiments—was calculated with

$$FE_i = \frac{P \times v \times c_i \times F \times N_i}{R \times T \times j} \times 100\% \quad (3)$$

where v is the volumetric flow rate of effluent gas measured using a digital flowmeter (Optiflow 520, Sigma-Aldrich), c_i is the concentration of the gas product species i measured by the GC, P is the atmospheric pressure (101.31 kPa), N_i is the number of electrons required to form one mole of that product by CO_2R and equal to 2 for both H_2 and CO, and j is the total current recorded by the potentiostat.

The production of formate was determined by a semibatch method by measuring the concentration of formate in the liquid at the end of a CO_2R experiment for about 35 min using ^1H nuclear magnetic resonance (NMR) spectroscopy (Bruker Avance 500 high-resolution NMR interfaced to an 11.7 Tesla 51 mm bore magnet system). Liquid samples were prepared for the NMR analysis by mixing 400 μL of the spent catholyte in 200 μL of heavy water (D_2O, 99.9 atom% D, Sigma-Aldrich) mixed with 0.05 vol % dimethyl sulfoxide (DMSO, ≥99%, Sigma-Aldrich) as the internal standard.

The FE_{HCOO-} of formate was calculated by

$$FE_{HCOO^-} = \frac{Q_{HCOO^-}}{Q_{total}} \times 100\% = \frac{C_{HCOO^-} \times V_{catholyte} \times F \times N_{HCOO^-}}{Q_{total}} \times 100\% \quad (4)$$

where C_{HCOO^-} is the concentration of formate in the catholyte determined by NMR, $V_{catholyte}$ is the total volume of catholyte in the H-cell (70 mL), N_{HCOO^-} is 2, and Q_{total} is the total charge passed during the CO_2R measurement.

Material Characterizations. Scanning electron microscopy (SEM) was performed on a JOEL JSM-7100 microscope. X-ray photoelectron spectroscopy (XPS) was conducted on a Kratos Axis ULTRA X-ray photoelectron spectrometer with a 165 mm hemispherical electron energy analyzer and a monochromatic Al Kα (1486.6 eV) radiation source at 15 kV (10 mA). The XPS data were analyzed using CASA software and calibrated with reference to C 1s. X-ray diffraction (XRD) data were collected using a Rigaku SmartLab XRD equipped with a 9 kW Cu rotating anode source, operated at 45 kV and 200 mA. Diffraction patterns were recorded in Bragg Brentano

https://dx.doi.org/10.1021/acsami.0c00412
ACS Appl. Mater. Interfaces 2020, 12, 22760−22770

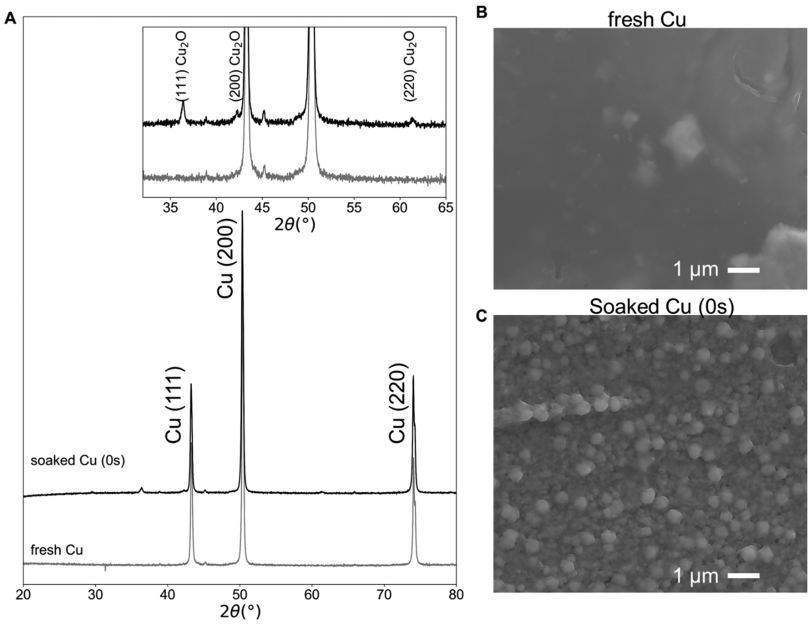

Figure 1. (A) X-ray diffraction (XRD) patterns of fresh Cu foil and the Cu foil soaked (0 s) in 0.668 M Na_2SnO_3 + 0.375 M NaOH aqueous solution for 30 min. The part (A) inset highlights the presence of Cu_2O with facets of (111), (200), and (220) in the treated Cu foil.[32] Scanning electron micrographs of (B) fresh Cu foil and (C) soaked Cu foil.

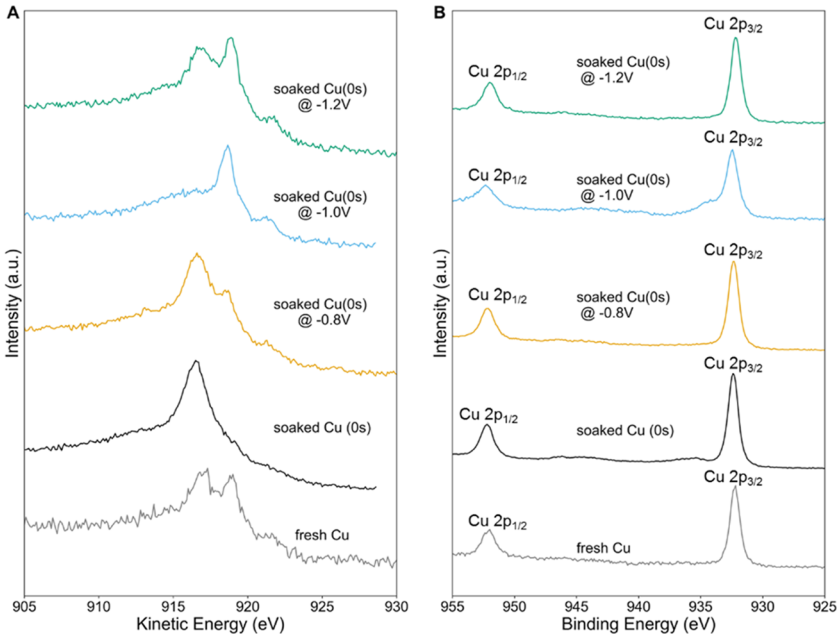

Figure 2. (A) Cu LMM Auger spectra and (B) X-ray photoelectron spectroscopy (XPS) spectra of Cu on the surface of fresh Cu, soaked Cu (0 s), and soaked Cu (0 s) that was used for 20 min as a cathode for CO_2 reduction in a CO_2-saturated 0.5 M $KHCO_3$ at −0.8 V, −1.0 V, and −1.2 V vs RHE.

mode by continuous scans from 5 to 90° 2Θ, with a step size of 0.02° at a scan rate of 2.5° per minute. The resulting patterns were imported into Diffrac EVA, version 4.2, where phases were identified using the PDF-4 2020 ICDD database. We estimated the electrochemically active surface area (ECSA) of cathodes in the H-cell by performing cyclic voltammetric (CV) analysis at voltage scan rates between 0.01 and 0.09 V s^{-1} over a 0.1 V electrochemical window in the non-Faradaic region in a CO_2-saturated 0.5 M $KHCO_3$ aqueous solution. The scan rates for the CVs were controlled in the range. The double-layer capacitances were calculated from the slopes of the capacitive current at open-circuit potential vs the scan rate, as derived from the cyclic voltammetry results. Subsequently, we divided the capacitance by 0.029 mF cm^{-2}, which is widely believed to be the specific capacitance for Sn-based materials.[19]

RESULTS AND DISCUSSION

The X-ray diffraction spectra in Figure 1A, and the inset for 2θ in the range of 34−65°, shows a layer of Cu_2O on the surface of the polished Cu foil that was soaked for 30 min in the 0.668 M Na_2SnO_3 and 0.375 M NaOH aqueous solutions. The XRD patterns indicate that the major facets of this Cu_2O phase are (111), (200), and (220).[32] After the 30 min soaking treatment, we also observed by scanning electron microscopy (SEM)

https://dx.doi.org/10.1021/acsami.0c00412
ACS Appl. Mater. Interfaces 2020, 12, 22760−22770

micrographs that the smooth surface of the polished Cu foil (Figure 1B) became rougher with 300−500 nm sized particles uniformly covering the surface of the soaked Cu (0 s) sample (Figure 1C). The formation of the Cu_2O layer is consistent with previous reports by Mackay et al.[33] and Zhang et al.[34]

We used the modified Auger parameter, which is the sum of the kinetic energy of the Cu LMM Auger peaks (Figure 2A) and the binding energy of the Cu $2p_{3/2}$ peak (Figure 2B), to distinguish the Cu^+ and metallic Cu. Table 1 shows the fresh Cu foil exhibited two modified Auger parameters at 1851.2 eV corresponding to metallic Cu and 1849.2 eV corresponding to Cu^+ species.[35] The latter Cu^+ species observed on fresh Cu is likely due to the exposure of the polished foil to air during handling and transfer to the XPS instrument. After soaking in the Na_2SnO_3 + NaOH solution for 30 min, only the modified Auger parameter 1848.9 eV of Cu^+ was observed, which suggests that the surface of the Cu foil was completely oxidized to Cu^+-based species. These XPS interpretations are consistent with the XRD (Figure 1A) and particles observed in the SEM (Figure 1C).

Table 1. Cu $2p_{3/2}$ Binding Energies, LMM Auger Kinetic Energies, and Modified Auger Parameters of Cu Foils

samples	Cu $2p_{3/2}$ binding energy (eV)	Cu LMM Auger kinetic energy (eV)		Cu modified Auger parameter (eV)	
		Cu^0	Cu^+	Cu^0	Cu^+
Cu foil	932.5	918.7	916.7	1851.2	1849.2
soaked Cu foil—0 s electrodeposition	932.1		916.8		1848.9
soaked Cu foil—0 s after CO_2R at −0.8 V in 0.5 M $KHCO_3$	932.3	918.7	916.7	1851.0	1849.0
soaked Cu foil—0 s after CO_2R at −1.0 V in 0.5 M $KHCO_3$	932.3	918.6	916.6	1850.9	1848.9
soaked Cu foil—0 s after CO_2R at −1.2 V in 0.5 M $KHCO_3$	932.1	919.0	917.0	1851.1	1849.1

We also examined how the surface chemistry of the soaked Cu foil changes after subject to CO_2R reaction conditions using this foil as a cathode at −0.8, −1.0, and −1.2 V vs RHE in a CO_2-saturated 0.5 M $KHCO_3$ solution for 20 min. The results are shown in Figure 2. The modified Auger parameters at 1848.9−1849.1 eV (Table 1) for these treated samples suggest that the Cu^+ species persist on the soaked Cu surface after exposure to CO_2R reaction conditions. This finding is consistent with the observations of Mistry et al.,[30] who reported the presence of Cu^+ when being treated at −0.91 V vs RHE for 1 h. The deconvoluted O 1s XPS peak (Figure S1) at ∼530.2 eV is related to the lattice oxygen, and the one at ∼531.6 eV is related to the oxygen of Cu2O defective oxide.[36] These two characteristic O 1s peaks further confirm the presence of Cu^+ species on the surface after the electrochemical treatment.

Figure 3 compares the microstructure of the deposited tin layer at the Cu foil. The Sn particles were deposited onto the surface of the soaked Cu 0 s sample after only 20 s deposition (shown in Figure 3A). The size of the Sn particles grew to approximately 100 nm (Figure 3B) after a 30 s deposition time. The surface of the 30 s sample became smoother as a result of the growth of Sn nuclei. The Cu nanoparticles have a higher density of low-coordinated sites such as corners and edges that can bind more strongly with adatoms than the flat surfaces.[37] These particles also exhibit a high electric field due to their large curvature.[38] Both could lead the Sn to deposit onto the formed Cu_2O-derived nanoparticles. The Sn nuclei deposited at the Cu particles started to coarsen between 30 s and 60 s (Figure 3D) and formed a continuous layer to fully cover the Cu foil surface after 120 s deposition time (Figure 3E). A deposition time longer than 120 s led to the formation of a prism-shaped microstructure on top of the continuous layer (Figure 3F).

The back-scattered electron (BSE) micrographs and energy-dispersive X-ray spectroscopy (EDS) spectra from SEM in Figure 4 provide further information about the distribution of Sn/Cu elements and the thickness of Sn deposited on the Cu foils. We selected samples deposited at 20, 30, 60, 120, and 684 s as the primary samples for this characterization. The specimen for this characterization was prepared by cutting the samples and subsequently mounting vertically in the epoxy with the cross section exposed to the top. In the BSE micrograph, atoms with a high atomic number show a high intensity of the BSE signal.[39,40] As Sn has an atomic number of 50 that is higher than that of Cu (29), in the BSE images (Figure 4A−E), the slightly bright layer at the left of images is

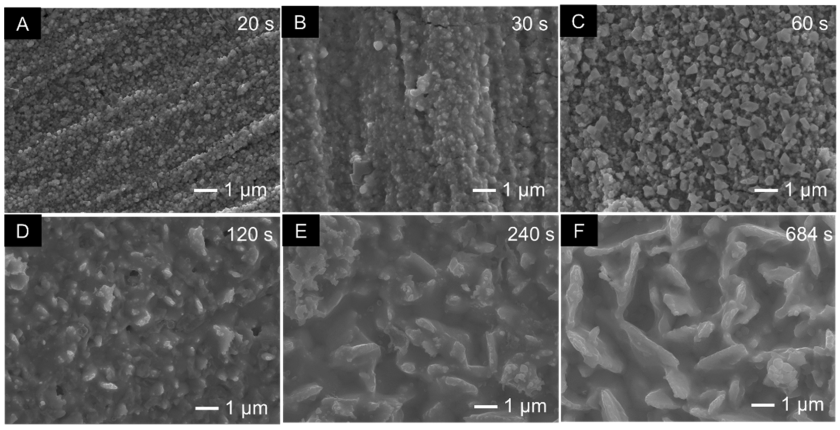

Figure 3. Scanning electron micrographs of the surface microstructure of the Sn-deposited Cu foil with deposition times of (A) 20 s, (B) 30 s, (C) 60 s, (D) 120 s, (E) 240 s, and (F) 684 s.

https://dx.doi.org/10.1021/acsami.0c00412
ACS Appl. Mater. Interfaces 2020, 12, 22760−22770

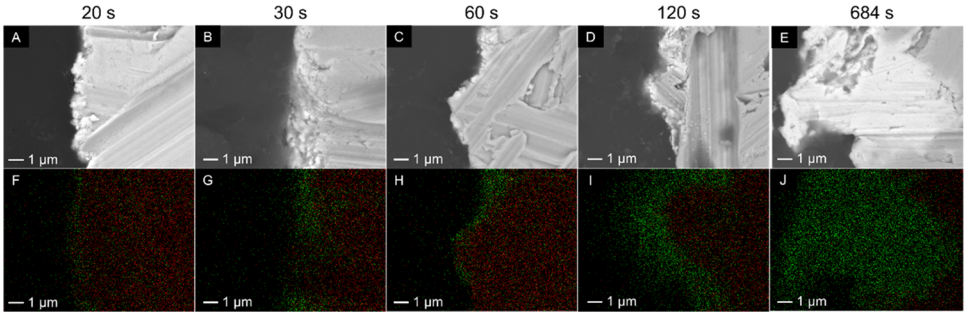

Figure 4. Back-scattered electron (BSE) micrographs of the cross-sections of the Cu foils deposited with Sn for (A) 20 s, (B) 30 s, (C) 60 s, (D) 120 s, and (E) 684 s. The corresponding energy-dispersive X-ray spectroscopy (EDS) mapping of Sn (green) and Cu (red) for (F) 20 s, (G) 30 s, (H) 60 s, (I) 120 s, and (J) 684 s.

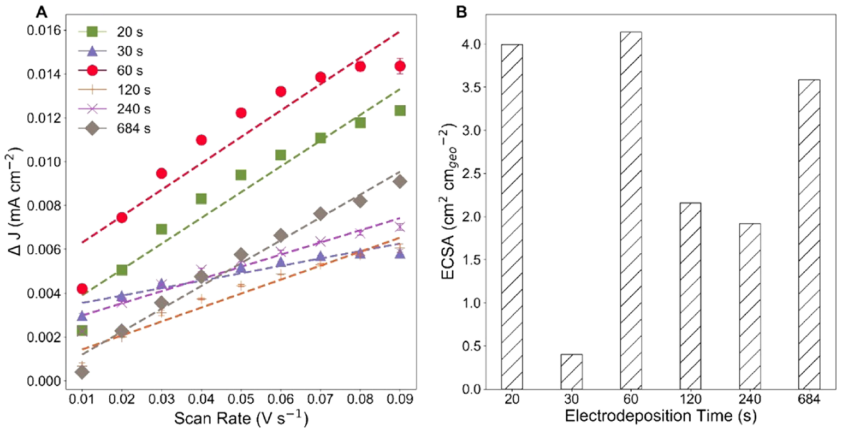

Figure 5. (A) Comparison of the capacitive current as a function of scan rate and (B) estimated electrochemically active surface area (ECSA) over Cu foils deposited with Sn for 20, 30, 60, 120, 240, and 684 s.

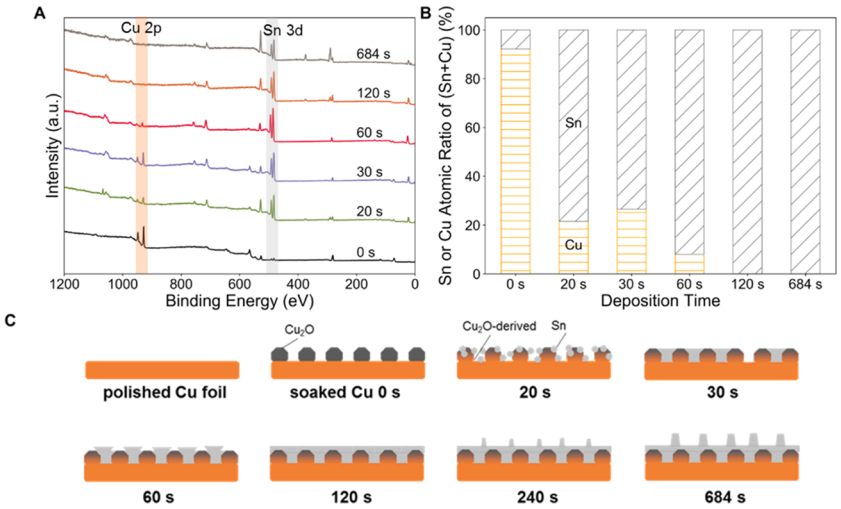

Figure 6. Comparison of (A) general surveys of XPS and (B) (Sn, Cu)/(Sn + Cu) atomic ratios on the surface of 0, 20, 30, 60, 120, and 684 s samples. (C) Schematic illustration of the processes of Sn electrodeposition over the Cu_2O-derived substrate.

Sn deposited on the surface of the foil and the slightly darker layers are the Cu atoms in the foil. The EDS elemental maps (Figure 4F−G) show Sn in green and Cu in red to confirm the deposition of Sn over the Cu surface.

Generally, the thickness of the Sn layer increased with an increase in deposition time. Consistent with the SEM microstructures shown in Figure 3, a deposition time less than 120 s leads to a discontinuous Sn layer, and the BSE shows that these layers were less than 1 μm thick. An electrodeposition time longer than 120 s produced a near-continuous Sn layer to fully cover the Cu substrate (Figure 4I). The prism-shaped protrusion was observed in Figure 4G for the 684 s sample, where the thickness of the Sn prism is around 10 μm. Therefore, the deposition time manipulates the contact interface between the Cu substrate and the Sn layer. The surface Sn layer has sufficient contact with the Cu atoms at a relatively short deposition time (i.e., 20, 30, and 60 s) and gradually lose such contact when the deposition time increases.

https://dx.doi.org/10.1021/acsami.0c00412
ACS Appl. Mater. Interfaces 2020, 12, 22760−22770

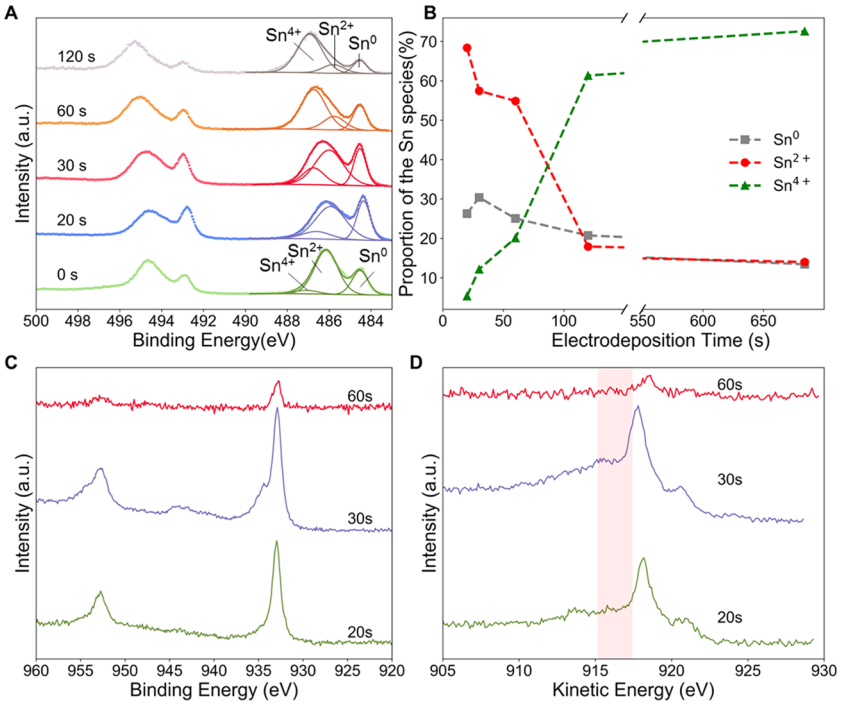

Figure 7. (A) High-resolution Sn 3d XPS spectra, (B) population of metallic Sn, Sn^{2+}, and Sn^{4+} on the surface for samples deposited with Sn for 20, 30, 60, 120, and 684 s. High-resolution Cu 2p XPS spectra (C) and (D) Cu LMM Auger spectra for 20, 30, and 60 s deposited Sn samples. The red region highlights the Auger peak located at a kinetic energy of ∼916 eV. All of the samples were treated at −0.8 V vs RHE in CO_2-saturated 0.5 M $KHCO_3$ for 20 min.

At 684 s, the Sn atom on the surface of ∼10 μm thick Sn prism protrusion is unlikely affected by its Cu substrate.

Figure 5A shows the capacitive current density of the Sn-coated Cu_2O-derived electrodes at scan rates of 0.01−0.09 V s^{-1} in 0.5 M $KHCO_3$, which were used to calculate the electrochemically active surface areas (ECSAs) in Figure 5B. The cyclic voltammograms to plot Figure 5A are shown in Figure S2. The ECSA results for the different Sn deposition times are consistent with the morphologies observed in the SEM images (Figure 3). The formation of Cu_2O nanoparticles may partially contribute to the high ECSA for samples with deposition times of 20 and 30 s. With an increase in deposition time, the surface was smoothed by the full coverage of the initial layer of Sn nuclei at the nanostructured Cu surface (Figure 3B). This smoothed surface led to the lowest ECSA of ∼0.4 cm^2 cm_{geo}^{-2} over the 30 s sample. With deposition time increasing, the Sn grew onto the first layer of Sn nuclei and made the surface rough again (ECSA (60 s) = ∼4 cm^2 cm_{geo}^{-2}) until the formation of the continuous Sn layer at around 120 s. After the formation of the continuous layer of Sn, the prism-shaped protrusions (Figure 2E−G) thereafter became the major contributor to the increase in the ECSA for samples >240 s.

In the general surveys of XPS (Figure 6A), we detected a small amount of Sn (<8%) on the soaked Cu foil. As the solution to prepare the soaked Cu contains Na_2SnO_3, the Sn element on the surface of the soaked Cu could be due to the Sn residues trapped in the rough Cu_2O layer. After electrodeposition at −72 mA cm^{-2} in the Na_2SnO_3 + NaOH, we observed a significant amount of Sn on the surface. The Cu species were detected on the surface of 20, 30, and 60 s Sn-coated samples, as evidenced by the Cu 2p characteristic peak at a binding energy of around 933 eV (Figure 6A). The absence of the Cu 2p peaks in samples with deposition times longer than 120 s suggests that after 120 s the Sn layer fully covers the Cu surface, as also observed from Figures 3D and 4D,I. The atomic population of Cu or Sn on the surface (Figure 6B), as quantified from these XPS spectra, also confirms that Cu species still exist on the surface when the deposition time is shorter than 120 s. This result is also consistent with what we observed in SEM micrographs in Figure 3 and EDS mapping in Figure 4. Overall, the coverage of Cu decreases with deposition time increasing from 20/30 to 60 s. The higher concentration of Cu in the 30 s sample than that in the 20 s sample highlights the discontinued Sn layer that may cause local variations of Cu/Sn dispersion on the surface. Figure 6C shows an illustration of the processes for Sn electrodeposition over the Cu_2O-derived substrate.

The X-ray diffraction patterns of the Sn-deposited samples, as shown in Figure S3A, revealed that the Sn species majorly include the Sn metal and SnO, Cu_3Sn alloy phases. In particular, the diffraction peak associated with the Cu_3Sn(121) facet becomes prominent when the deposition time increases up to 240−684 s. As Sn fully covers the surface with deposition times longer than 120 s, these prominent Cu_3Sn alloy phases should be formed below the sample surfaces of the 120, 240, and 684 s samples. Additionally, minor diffraction peaks related to Cu_2O(111) and (220) are still present in Sn-deposited samples at 2θ = ∼36 and 61.5°, respectively (see Figure S3B,C), indicating the presence of Cu_2O phases after Sn electrodeposition.

It is widely reported that the selectivity of CO_2R toward formate depends upon the oxidation state of the Sn species on the surface of the cathode.[12,13,15−17] The high-resolution XPS over the Sn $3d_{5/2}$ shows the oxidation states of Sn on the surface after being used as a cathode for 20 min to catalyze CO_2R at −0.8 V vs RHE in a CO_2-saturated 0.5 M $KHCO_3$. After the cathodic CO_2R treatment, the samples were quickly

https://dx.doi.org/10.1021/acsami.0c00412
ACS Appl. Mater. Interfaces 2020, 12, 22760−22770

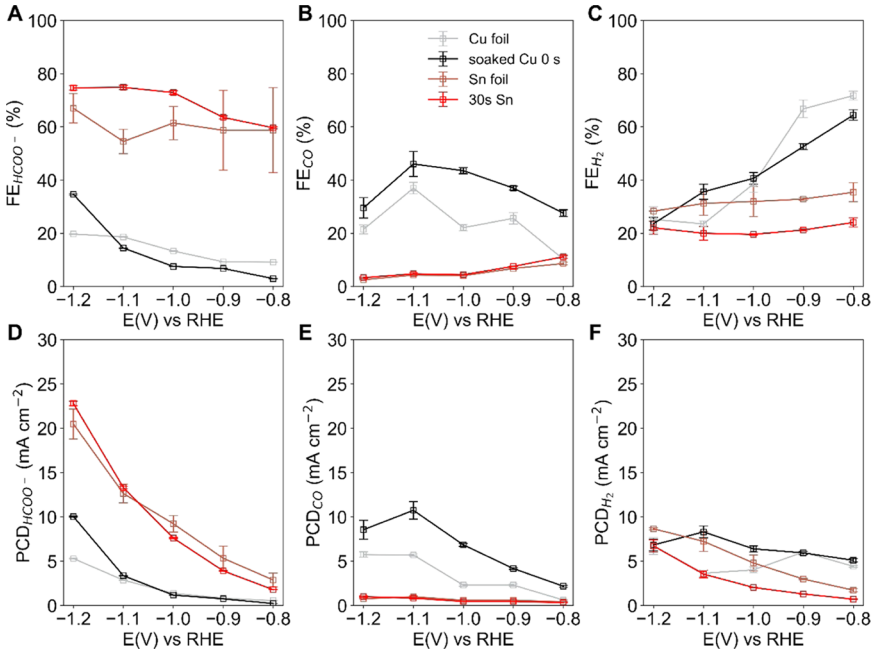

Figure 8. Comparison of the Faradaic efficiency (FE) of (A) formate, (B) CO, and (C) H_2 and partial current density (PCD) of (D) formate, (E) CO, and (F) H_2 as a function of potential over the Cu foil, 0 s sample, Sn foil, and 30 s deposited electrode in the CO_2-saturated 0.5 M $KHCO_3$ aqueous electrolyte.

cleaned with deionized water, dried, stored in CO_2-filled vials, and transferred for XPS measurement. Figure 7A shows the XPS spectra of Sn $3d_{5/2}$ deconvoluted into three major peaks at binding energies of ca. 486.7 eV for Sn^{4+}, ca. 485.9 eV for Sn^{2+}, and ca. 484.6 eV for metallic Sn.[14] Figure 7B compares the proportions of Sn species on the surface for different electrodeposition times and shows that longer Sn deposition times increased the concentration of Sn^{4+} and decreased the concentrations of Sn^{2+} on the surface. The concentration of the metallic Sn species was similar in all of the tested samples. Note that the samples were treated under CO_2R conditions in the order 20, 30, 60, 120, and 684 s and then taken to the XPS instrument in a batch, and therefore, the samples with shorter deposition times are likely to be more oxidized through a longer potential exposure to air. As such, we could rule out the effect of the testing sequence and confirm that the surface Sn was more oxidized on the surface of samples with longer deposition times. More specifically, such an impact from the deposition duration is more prominent below 120 s than the ones prepared longer than 120 s, as below 120 s the surface Sn layer has sufficient contact with exposed cuprous species on the surface or from the subsurface below the Sn layer; such a Sn−Cu contact is likely the main reason for the significant variation in the Sn oxidation state on the surface.

As Cu species was still observed on foils with electrodeposition times of 20, 30, and 60 s, we examined the high-resolution Cu 2p XPS spectra (Figure 7A) and LMM Auger spectra (Figure 7D) on these foils. After deposited with Sn and treated under the CO_2R condition, the Cu_2O formed during the soaking process was majorly reduced into metallic Cu, as evidenced from the major Auger peak at a kinetic energy of 918.7 eV, which corresponds to a modified Auger parameter close to 1851.2 eV (i.e., metallic Cu). However, in Figure 7D, the Auger peak at a kinetic energy of 916.5 eV (highlighted in the red region, a modified Auger parameter of ca. 1849.2 eV) shows the presence of Cu^+ species after Sn deposition and then CO_2R treatment for 20 and 30 s Sn-coated foils. For the sample with deposition time longer than 60 s, the Cu signal is relatively weak in both the XPS and Auger spectra because most of this surface is covered by Sn and fewer Cu atoms are exposed. Nevertheless, the Auger broad spectra (Figure 6F) still show an extra peak at a kinetic energy of around 916.5 eV that could be due to the presence of Cu^+. The O 1s XPS spectra (shown in Figure S4) also exhibit the deconvoluted Cu_2O characteristic peaks at ∼530.2 eV (lattice oxygen) and ∼531.6 eV (oxygen of the defective oxide).[36] Therefore, we could conclude that Cu^+ can be present on the surface or subsurface in contact with the deposited Sn species.

Considering the unique electronegativity of Cu^+ (1.56) that is between 1.73 for Sn^{4+} and 1.34 for Sn^{2+},[29] we postulated that the cuprous species formed from soaking treatment affects the oxidation state of Sn atoms on the surface. The less electronegative Cu^+ than Sn^{4+} prevents the oxidation of surface Sn from 4+ through donating electrons to its neighboring Sn atoms, while the Cu^+ atoms withdraw electrons when Sn is in +2 state due to its relatively high electronegativity. Such phenomena can be well exemplified by the Sn deposited for 20, 30, 60, and 120 s, as presented in Figure 7B, where the area of contact interface between surface Sn and Cu is sufficient. For samples with longer deposition times than 120 s, most of the Sn surface layer is in contact with Sn species and thus is not significantly affected by the Cu substrate.

The electrodes were evaluated in a custom-made H-cell with a proton-conducting Nafion 117 membrane separating the cathode and anode chambers. The samples were tested at the cathode chamber in a CO_2-saturated 0.5 M $KHCO_3$ electrolyte. Cyclic voltammograms over 30 s—the deposited Sn electrode (Figure S5) showed that the current density in 0.5 M $KHCO_3$ saturated with CO_2 is higher than that in the Ar-saturated electrolyte, suggesting that CO_2R occurred on the electrode surface. The major products from the test include formate ($HCOO^-$), CO, and H_2, and the total measured

https://dx.doi.org/10.1021/acsami.0c00412
ACS Appl. Mater. Interfaces 2020, 12, 22760−22770

overall FEs of these products are within 90−100%. We detected a small amount of CH_4 (FE < 0.5%) and C_2H_4 (FE < 0.3%) at −0.8 V vs RHE for 20, 30, and 60 s deposited Sn, and the FEs of these two products decrease with the Sn electrodeposition time (Figure S6). As the Cu is the only known metal that can produce a sufficient amount of CH_4 and C_2H_4, the production of CH_4 and C_2H_4 likely arises from the exposure of the Cu species on the surface.

We compared the Faradaic efficiency (FE, shown in Figure 8A−C) and partial current density (PCD, shown in Figure 8D−F) of formate (i.e., $HCOO^-$), CO, and H_2 over the 30 s deposited Sn electrode over the Cu foil, 0 s sample, and Sn foil electrodes. As shown in Figure 8A, the deposited Sn electrode shows a much higher FE of $HCOO^-$ than those of the Cu foil and 0 s sample. This highlights the essential role of deposited Sn species in the formation of $HCOO^-$. Interestingly, the deposited Sn exhibits a more selective CO_2 conversion to formate, especially at a more negative potential. For example, the deposited Sn electrode shows a FE_{HCOO^-} of ∼75%, much higher than that over the Sn foil (FE_{HCOO^-} = 55%) at −1.1 V vs RHE. The FE_{CO} is the lowest for both Sn-based electrodes and shows the negligible difference between deposited Sn and Sn foil (Figure 8B). Additionally, the deposited Sn electrode is more useful to suppress the unwanted HER, as evidenced by the lowest FE(H_2) shown in Figure 8C. Correspondingly, the PCD of HER over the Sn-deposited electrode is also the lowest among all of the tested electrodes. The overall FE for CO_2R to produce C1 products, including $HCOO^-$ and CO product, is ∼80% over the Sn-deposited electrode, more than one-third higher than the FE(C1) over the Sn foil.

The FE_{HCOO^-} of the 30 s sample is also higher than the reported values over Cu−Sn alloys, including Cu_3Sn (FE_{HCOO^-} = ∼40% at −1.09 V vs RHE)[41] and $Cu_{76}Sn_{24}$ (FE_{HCOO^-} = ∼54% at −1.1 V vs RHE).[42] The higher FE_{HCOO^-} over the 30 s Sn-deposited sample than over the Cu−Sn alloy means that the Cu_3Sn alloy phase is not the key active sites for the selective CO_2R catalysis. The effective promotion of formate and suppression of the HER likely arises from the Sn/SnOx interfaces, which was also recently reported by An et al.[17] As aforementioned, 30 s deposited Sn has sufficient contact with the nanostructured surface of the 0 s sample where Cu^+ species are present. Due to the unique electronegativity of Cu^+, the Cu^+ stabilizes the oxidation state of the surface Sn majorly in +2, which was also confirmed by the XPS result shown in Figure 6D.

The role of the Cu^+ in the tin-deposited electrode was further investigated by comparing the FE ($HCOO^-$) at potentials between −0.8 and −1.1 V vs RHE as a function of the deposition time. Figure 9 summarizes the results. The electrodes with a Sn deposition duration between 30 and 120 s show the highest selectivity toward formate among all the electrodes under the tested potentials. For example, the 60 s deposited Sn electrode enables an FE ($HCOO^-$) up to ∼80% at −1.0 V vs RHE (PCD_{HCOO^-} = 11.8 mA cm^{-2}, overpotential = 580 mV) and the 120 s sample shows an FE($HCOO^-$) of ∼81% at −1.1 V vs RHE (PCD_{HCOO^-} = 17.6 mA cm^{-2}, overpotential = 680 mV). Both FEs of $HCOO^-$ are more than one-third higher than that over the Sn foil at similar potentials. Table S1 shows that the FE_{HCOO^-} values of 60 and 120 s samples are comparable to some of the state-of-the-art Sn-based nanostructured catalysts such as $Bi_{0.57}Sn_{0.43}$ alloy (FE = 78% at −1.1 V vs RHE)[43] and Cu/SnO_2 core−shell nanoparticles (FE = 65% at −1.0 V vs RHE).[44] In contrast,

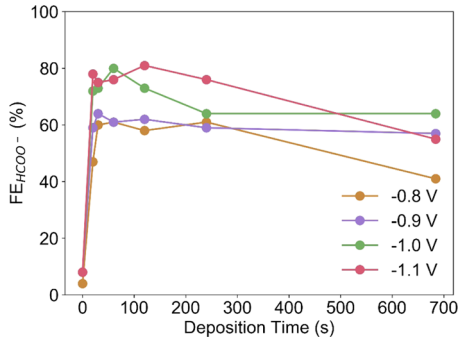

Figure 9. Comparison of FE to produce formate at −0.8, −0.9, −1.0, and −1.1 V vs RHE as a function of the Sn deposition duration from 0 to 684 s.

the Sn electrode deposited for 684 s only shows 41−64% FE($HCOO^-$) at −0.8 to −1.1 V vs RHE, which is very similar to that of the Sn foil (FE($HCOO^-$) = 59−61%) at the same potential range. Such similarity illustrates that the substrate has no impact on the selectivity of the 684 s sample, where the surface Sn has nearly no contact with the Cu substrate (Figure 4E,G). Although the Sn−Cu alloys have been reported to promote CO_2R,[19] the absence of Cu on the surface for the 120 s sample (Figure 5A,B) ruled out the potential beneficial alloying effects on the CO_2R. As reported by Dutta et al.[16] and An et al.,[17] the Sn species in 2+ and 4+ are active to produce formate. Therefore, the Sn electrode with a relatively short deposition duration has an optimal concentration of both Sn^{2+} and Sn^{4+}, as demonstrated in Figure 6D, which likely contributed to the enhanced selectivity of the formate. Such an optimal concentration of CO_2R-active Sn species mainly arises from the regulating effects of the cuprous species that could maintain an optimal oxidation state of Sn via its moderate electronegativity.

We also performed a short-term stability measurement over the 30 s deposited Sn and Sn foil in the H-cell for 5 h. Figure 10 compares the FE of $HCOO^-$, CO, and H_2 and the PCD of $HCOO^-$ as a function of the time at −1.1 V vs RHE over these two electrodes. Because H_2, CO, and formate constitute nearly 100% of the FE, we approximated the FE of formate by subtracting 100% by FEs of H_2 and CO determined by the GC analysis. Although the FE of formate over deposited Sn slightly decreased with time from ∼80 to ∼75% accompanied by a slight increase in HER, the PCD of formate remains nearly unchanged, likely due to a slight increase in the overall current density (Figure 10A). The SEM micrographs (Figure S7) show that the particles on the surface of 30 s deposited Sn coarsened after the stability test, while the surfaces of Sn and Cu foil became slightly rough after the same treatment. Analyses of the Sn 3d XPS spectra results (Figure S8) indicate that the oxidation states of the surface Sn did not change significantly after the stability test as compared with the one treated at −0.8 V vs RHE for 20 min. Since the reaction took place in a batch mode operation, where the local environment, such as temperature, cation concentration, and pH, changes with time, and may also contribute to the degradation of the selectivity of the CO_2R.[31] All of these changes could contribute to the degradation of the performance of the Sn-deposited samples. Nevertheless, the deposited Sn over the CuO_2-derived substrate demonstrated higher stability than the Sn foil (Figure 10B), whose FE of $HCOO^-$ decreased from ∼79 to 65% and H_2 increased from ∼19 to ∼33%.

https://dx.doi.org/10.1021/acsami.0c00412
ACS Appl. Mater. Interfaces 2020, 12, 22760−22770

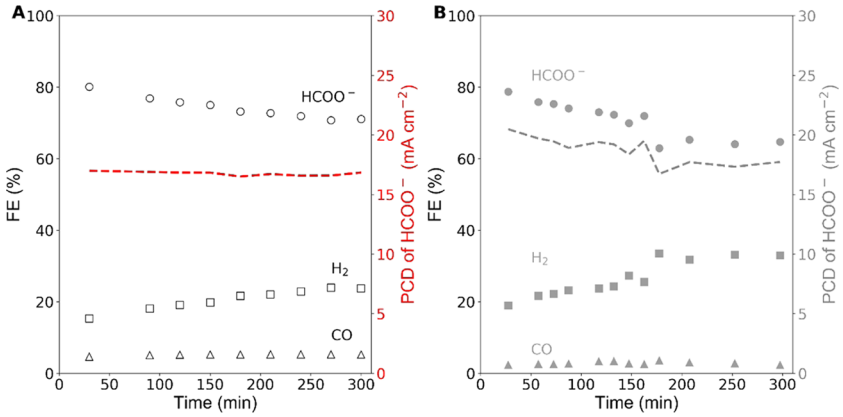

Figure 10. FEs of CO, H_2, and calculated FE of formate and partial current density of formate as a function of time over (A) 30 s deposited Sn electrode and (B) Sn foil electrode.

CONCLUSIONS

In summary, we deposited Sn onto the Cu_2O-derived surface for varied deposition durations and evaluated them as the cathode electrodes to catalyze the CO_2 electrochemical reduction to produce formate in an H-cell. Although the Sn is the major contributor to the formate production, only a relatively short deposition duration of less than 120 s leads to a selective formate conversion and suppressed the hydrogen evolution reaction. This result highlights the significant role of the Cu_2O-derived substrate in determining the catalytic selectivity over the deposited Sn catalyst. The results of our surface analysis revealed that Cu^+ likely exists on the surface or at the subsurface during the cathodic Sn deposition and CO_2R due to the kinetic limitations on the surface. Cu^+ has a moderate electronegativity higher than Sn^{2+} but lower than that of Sn^{4+}. When the deposition duration is below 120 s, where there is sufficient contact interface between Sn and Cu, the remaining Cu^+ species can stabilize the surface Sn at a relatively positive oxidation state between +2 and +4 by donating charge to Sn^{4+} and withdrawing charge from Sn^{2+}. Such a unique modulation effect of Cu^+ in the substrate contributed to the observed improved catalytic selectivity over the Sn-deposited electrode. Our work also highlights the significant roles of the substrate in the electrocatalytic selectivity of the catalyst and provides an effective alternative strategy to advance selective electrocatalysis by engineering the substrate.

ASSOCIATED CONTENT

Supporting Information

The Supporting Information is available free of charge at https://pubs.acs.org/doi/10.1021/acsami.0c00412.

O 1s on the surface of fresh Cu, soaked Cu (0 s), and the soaked Cu (0 s) used as cathode under various potentials; cyclic voltammetry at different scan rates for Sn-deposited samples; XRD spectra of Sn deposited Cu samples; high-resolution O 1s XPS spectra; comparison of cyclic voltammograms for 30 s Sn-deposited catalyst; comparison of the FE(CH_4) and FE(C_2H_4); SEM images of Sn, Cu and Sn 30 s; and comparison of Sn 3d high-resolution XPS spectra and corresponding surface Sn oxidation states (PDF)

AUTHOR INFORMATION

Corresponding Authors

Mengran Li − *School of Chemical Engineering, The University of Queensland, 4072 Brisbane, Queensland, Australia;* orcid.org/0000-0001-7858-0533; Email: m.li6@uq.edu.au

Thomas E. Rufford − *School of Chemical Engineering, The University of Queensland, 4072 Brisbane, Queensland, Australia;* orcid.org/0000-0002-8865-7976; Email: t.rufford@uq.edu.au

Authors

Xiaohe Tian − *School of Chemical Engineering, The University of Queensland, 4072 Brisbane, Queensland, Australia*

Sahil Garg − *School of Chemical Engineering, The University of Queensland, 4072 Brisbane, Queensland, Australia*

Peiyao Zhao − *Department of Chemical Engineering, University of Massachusetts Amherst, Amherst, Massachusetts 01003, United States*

Yuming Wu − *School of Chemical Engineering, The University of Queensland, 4072 Brisbane, Queensland, Australia*

Anya Josefa Yago − *Centre for Microscopy and Microanalysis, The University of Queensland, 4072 Brisbane, Queensland, Australia*

Lei Ge − *School of Chemical Engineering, The University of Queensland, 4072 Brisbane, Queensland, Australia; Centre for Future Materials, The University of Southern Queensland, 4300 Springfield, Australia;* orcid.org/0000-0003-2989-0329

Victor Rudolph − *School of Chemical Engineering, The University of Queensland, 4072 Brisbane, Queensland, Australia*

Geoff Wang − *School of Chemical Engineering, The University of Queensland, 4072 Brisbane, Queensland, Australia*

Complete contact information is available at: https://pubs.acs.org/10.1021/acsami.0c00412

Author Contributions

[⊥]M.L. and X.T. contributed equally to this work.

Notes

The authors declare no competing financial interest.

ACKNOWLEDGMENTS

This research is financially supported by the HBIS Group and the Australian Research Council (ARC) Linkage Project No. LP160101729. S.G. acknowledges scholarship support by the University of Queensland (UQ) and the Australian Research Council's Centre for LNG Futures (IC150100019). Y.W.

acknowledges the financial support provided by the UQ Research Training Program (RTP) scholarship. We acknowledge the technical support from the Centre for Microscopy and Microanalysis and the Centre for Advanced Imaging at UQ.

REFERENCES

(1) Bushuyev, O. S.; De Luna, P.; Dinh, C. T.; Tao, L.; Saur, G.; van de Lagemaat, J.; Kelley, S. O.; Sargent, E. H. What Should We Make with CO_2 and How Can We Make It? *Joule* **2018**, *2*, 825−832.

(2) Kauffman, D. R.; Thakkar, J.; Siva, R.; Matranga, C.; Ohodnicki, P. R.; Zeng, C.; Jin, R. Efficient Electrochemical CO_2 Conversion Powered by Renewable Energy. *ACS Appl. Mater. Interfaces* **2015**, *7*, 15626−15632.

(3) Garg, S.; Li, M.; Weber, A. Z.; Ge, L.; Li, L.; Rudolph, V.; Wang, G.; Rufford, T. E. Advances and Challenges in Electrochemical CO2 Reduction Processes: An Engineering and Design Perspective Looking Beyond New Catalyst Materials. *J. Mater. Chem. A* **2020**, *8*, 1511−1544.

(4) Oloman, C.; Li, H. Electrochemical Processing of Carbon Dioxide. *ChemSusChem* **2008**, *1*, 385−391.

(5) Qiao, J.; Liu, Y.; Hong, F.; Zhang, J. A Review of Catalysts for the Electroreduction of Carbon Dioxide to Produce Low-carbon Fuels. *Chem. Soc. Rev.* **2014**, *43*, 631−675.

(6) Nitopi, S.; Bertheussen, E.; Scott, S. B.; Liu, X.; Engstfeld, A. K.; Horch, S.; Seger, B.; Stephens, I. E. L.; Chan, K.; Hahn, C.; Nørskov, J. K.; Jaramillo, T. F.; Chorkendorff, I. Progress and Perspectives of Electrochemical CO2 Reduction on Copper in Aqueous Electrolyte. *Chem. Rev.* **2019**, *119*, 7610−7672.

(7) Afshar, A. A. N.*Chemical Profile: Formic Acid*; TranTech Consultants, Inc., 2014.

(8) Fan, L.; Xia, Z.; Xu, M.; Lu, Y.; Li, Z. 1D SnO2 with Wire-in-Tube Architectures for Highly Selective Electrochemical Reduction of CO2 to C1 Products. *Adv. Funct. Mater.* **2018**, *28*, No. 1706289.

(9) Lee, W.; Kim, Y. E.; Youn, M. H.; Jeong, S. K.; Park, K. T. Catholyte-Free Electrocatalytic CO2 Reduction to Formate. *Angew. Chem., Int. Ed.* **2018**, *57*, 6883−6887.

(10) Gu, J.; Héroguel, F.; Luterbacher, J.; Hu, X. Densely Packed, Ultra Small SnO Nanoparticles for Enhanced Activity and Selectivity in Electrochemical CO2 Reduction. *Angew. Chem., Int. Ed.* **2018**, *57*, 2943−2947.

(11) Zhao, S.; Li, S.; Guo, T.; Zhang, S.; Wang, J.; Wu, Y.; Chen, Y. Advances in Sn-Based Catalysts for Electrochemical CO2 Reduction. *Nano-Micro Lett.* **2019**, *11*, 62.

(12) Chen, Y.; Kanan, M. W. Tin Oxide Dependence of the CO_2 Reduction Efficiency on Tin Electrodes and Enhanced Activity for Tin/Tin Oxide Thin-Film Catalysts. *J. Am. Chem. Soc.* **2012**, *134*, 1986−1989.

(13) Li, Y.; Qiao, J.; Zhang, X.; Lei, T.; Girma, A.; Liu, Y.; Zhang, J. Rational Design and Synthesis of SnOx Electrocatalysts with Coralline Structure for Highly Improved Aqueous CO2 Reduction to Formate. *ChemElectroChem* **2016**, *3*, 1618−1628.

(14) Zhao, P.; Li, M.; Garg, S.; Tian, X.; Wang, G.; Rufford, T. E. Chlorine-modulated Tin Oxide as an Efficient Catalyst Toward Carbon Dioxide Electrochemical Reduction. In *Chemeca 2019: Chemical Engineering Megatrends and Elements*; Engineers Australia: Sydney, 2019.

(15) Baruch, M. F.; Pander, J. E.; White, J. L.; Bocarsly, A. B. Mechanistic Insights into the Reduction of CO2 on Tin Electrodes using in Situ ATR-IR Spectroscopy. *ACS Catal.* **2015**, *5*, 3148−3156.

(16) Dutta, A.; Kuzume, A.; Rahaman, M.; Vesztergom, S.; Broekmann, P. Monitoring the Chemical State of Catalysts for CO2 Electroreduction: An In Operando Study. *ACS Catal.* **2015**, *5*, 7498−7502.

(17) An, X.; Li, S.; Yoshida, A.; Wang, Z.; Hao, X.; Abudula, A.; Guan, G. Electrodeposition of Tin-Based Electrocatalysts with Different Surface Tin Species Distributions for Electrochemical Reduction of CO2 to HCOOH. *ACS Sustainable Chem. Eng.* **2019**, *7*, 9360−9368.

(18) Wang, Z.; Yang, C.; Guan, A.; Shang, L.; Al-Enizi, A. M.; Zhang, L.; Zheng, G. Sub-5 nm SnO2 Chemically Coupled Hollow Carbon Spheres for Efficient Electrocatalytic CO2 Reduction. *J. Mater. Chem. A* **2018**, *6*, 20121−20127.

(19) Zheng, X.; Ji, Y.; Tang, J.; Wang, J.; Liu, B.; Steinrück, H.-G.; Lim, K.; Li, Y.; Toney, M. F.; Chan, K.; Cui, Y. Theory-guided Sn/Cu Alloying for Efficient CO2 Electroreduction at Low Overpotentials. *Nat. Catal.* **2019**, *2*, 55−61.

(20) Liu, S.; Xiao, J.; Lu, X. F.; Wang, J.; Wang, X.; Lou, X. W. Efficient Electrochemical Reduction of CO_2 to HCOOH over Sub-2 nm SnO_2 Quantum Wires with Exposed Grain Boundaries. *Angew. Chem., Int. Ed.* **2019**, *58*, 8499−8503.

(21) Li, Q.; Rao, X.; Sheng, J.; Xu, J.; Yi, J.; Liu, Y.; Zhang, J. Energy Storage through CO2 Electroreduction: A Brief Review of Advanced Sn-based Electrocatalysts and Electrodes. *J. CO2 Util.* **2018**, *27*, 48−59.

(22) Mengran, L.; Garg, S.; Chang, X.; Ge, L.; Li, L.; Konarova, M.; Rufford, T. E.; Rudolph, V.; Wang, G. Towards Excellence of Transition Metals-based Catalysts for CO2 Electrochemical Reduction: An Overview of Strategies and Rationales. *Small Methods* **2020**, No. 2000033.

(23) Zheng, X.; De Luna, P.; García de Arquer, F. P.; Zhang, B.; Becknell, N.; Ross, M. B.; Li, Y.; Banis, M. N.; Li, Y.; Liu, M.; Voznyy, O.; Dinh, C. T.; Zhuang, T.; Stadler, P.; Cui, Y.; Du, X.; Yang, P.; Sargent, E. H. Sulfur-Modulated Tin Sites Enable Highly Selective Electrochemical Reduction of CO2 to Formate. *Joule* **2017**, *1*, 794−805.

(24) Liang, C.; Kim, B.; Yang, S.; Yang, L.; Francisco Woellner, C.; Li, Z.; Vajtai, R.; Yang, W.; Wu, J.; Kenis, P. J. A.; Ajayan, P. M. High Efficiency Electrochemical Reduction of CO2 Beyond the Two-electron Transfer Pathway on Grain Boundary Rich Ultra-small SnO2 Nanoparticles. *J. Mater. Chem. A* **2018**, *6*, 10313−10319.

(25) Li, F.; Chen, L.; Xue, M.; Williams, T.; Zhang, Y.; MacFarlane, D. R.; Zhang, J. Towards A Better Sn: Efficient Electrocatalytic Reduction of CO2 to Formate by Sn/SnS2 Derived from SnS2 Nanosheets. *Nano Energy* **2017**, *31*, 270−277.

(26) Li, M.; Zhao, M.; Li, F.; Zhou, W.; Peterson, V. K.; Xu, X.; Shao, Z.; Gentle, I.; Zhu, Z. A Niobium and Tantalum Co-doped Perovskite Cathode for Solid Oxide Fuel Cells Operating Below 500 °C. *Nat. Commun.* **2017**, *8*, No. 13990.

(27) Li, M.; Zhou, W.; Peterson, V. K.; Zhao, M.; Zhu, Z. A Comparative Study of SrCo0.8Nb0.2O3−δ and SrCo0.8Ta0.2O3−δ as Low-Temperature Solid Oxide Fuel Cell Cathodes: Effect of Non-geometry Factors on the Oxygen Reduction Reaction. *J. Mater. Chem. A* **2015**, *3*, 24064−24070.

(28) Rehman, A. U.; Li, M.; Knibbe, R.; Khan, M. S.; Peterson, V. K.; Brand, H. E. A.; Li, Z.; Zhou, W.; Zhu, Z. Enhancing Oxygen Reduction Reaction Activity and CO2 Tolerance of Cathode for Low-Temperature Solid Oxide Fuel Cells by in Situ Formation of Carbonates. *ACS Appl. Mater. Interfaces* **2019**, *11*, 26909−26919.

(29) Matar, S. F.; Campet, G.; Subramanian, M. A. Electronic Properties of Oxides: Chemical and Theoretical Approaches. *Prog. Solid State Chem.* **2011**, *39*, 70−95.

(30) Mistry, H.; Varela, A. S.; Bonifacio, C. S.; Zegkinoglou, I.; Sinev, I.; Choi, Y.-W.; Kisslinger, K.; Stach, E. A.; Yang, J. C.; Strasser, P.; Cuenya, B. R. Highly Selective Plasma-activated Copper Catalysts for Carbon Dioxide Reduction to Ethylene. *Nat. Commun.* **2016**, *7*, No. 12123.

(31) Garg, S.; Li, M.; Rufford, T. E.; Ge, L.; Rudolph, V.; Knibbe, R.; Konarova, M.; Wang, G. G. X. Catalyst−Electrolyte Interactions in Aqueous Reline Solutions for Highly Selective Electrochemical CO2 Reduction. *ChemSusChem* **2019**, *13*, 304−311.

(32) Marcos Esteban, R.; Meyer, H.; Kim, J.; Gemel, C.; Fischer, R. A.; Janiak, C. Comparative Synthesis of Cu and Cu2O Nanoparticles from Different Copper Precursors in an Ionic Liquid or Propylene Carbonate. *Eur. J. Inorg. Chem.* **2016**, *2016*, 2106−2113.

https://dx.doi.org/10.1021/acsami.0c00412
ACS Appl. Mater. Interfaces 2020, 12, 22760−22770

(33) Mackay, D. T.; Janish, M. T.; Sahaym, U.; Kotula, P. G.; Jungjohann, K. L.; Carter, C. B.; Norton, M. G. Template-free Electrochemical Synthesis of Tin Nanostructures. *J. Mater. Sci.* **2014**, *49*, 1476−1483.
(34) Zheng, J. Y.; Van, T.-K.; Pawar, A. U.; Kim, C. W.; Kang, Y. S. One-step Transformation of Cu to Cu2O in Alkaline Solution. *RSC Adv.* **2014**, *4*, 18616−18620.
(35) Biesinger, M. C.; Lau, L. W. M.; Gerson, A. R.; Smart, R. S. C. Resolving Surface Chemical States in XPS Analysis of First Row Transition Metals, Oxides and Hydroxides: Sc, Ti, V, Cu and Zn. *Appl. Surf. Sci.* **2010**, *257*, 887−898.
(36) Biesinger, M. C. Advanced Analysis of Copper X-ray Photoelectron Spectra. *Surf. Interface Anal.* **2017**, *49*, 1325−1334.
(37) Back, S.; Yeom, M. S.; Jung, Y. Active Sites of Au and Ag Nanoparticle Catalysts for CO2 Electroreduction to CO. *ACS Catal.* **2015**, *5*, 5089−5096.
(38) Popov, K. I.; Djokić, S. S.; Grgur, B. N. Springerlink. In *Fundamental Aspects of Electrometallurgy*, Boston, MA: Springer US, 2002.
(39) Rehman, A. U.; Li, M.; Knibbe, R.; Khan, M. S.; Zhou, W.; Zhu, Z. Unveiling Lithium Roles in Cobalt-Free Cathodes for Efficient Oxygen Reduction Reaction below 600 °C. *ChemElectroChem* **2019**, *6*, 5340−5348.
(40) Li, M.; Zhou, W.; Zhu, Z. Highly CO2-Tolerant Cathode for Intermediate-Temperature Solid Oxide Fuel Cells: Samarium-Doped Ceria-Protected SrCo0.85Ta0.15O3−δ Hybrid. *ACS Appl. Mater. Interfaces* **2017**, *9*, 2326−2333.
(41) Morimoto, M.; Takatsuji, Y.; Iikubo, S.; Kawano, S.; Sakakura, T.; Haruyama, T. Experimental and Theoretical Elucidation of Electrochemical CO2 Reduction on an Electrodeposited Cu3Sn Alloy. *J. Phys. Chem. C* **2019**, *123*, 3004−3010.
(42) Rasul, S.; Pugnant, A.; Xiang, H.; Fontmorin, J.-M.; Yu, E. H. Low Cost and Efficient Alloy Electrocatalysts for CO2 Reduction to Formate. *J. CO2 Util.* **2019**, *32*, 1−10.
(43) Tang, J.; Daiyan, R.; Ghasemian, M. B.; Idrus-Saidi, S. A.; Zavabeti, A.; Daeneke, T.; Yang, J.; Koshy, P.; Cheong, S.; Tilley, R. D.; Kaner, R. B.; Amal, R.; Kalantar-Zadeh, K. Advantages of Eutectic Alloys for Creating Catalysts in the Realm of Nanotechnology-enabled Metallurgy. *Nat. Commun.* **2019**, *10*, No. 4645.
(44) Li, Q.; Fu, J.; Zhu, W.; Chen, Z.; Shen, B.; Wu, L.; Xi, Z.; Wang, T.; Lu, G.; Zhu, J.-j.; Sun, S. Tuning Sn-Catalysis for Electrochemical Reduction of CO2 to CO via the Core/Shell Cu/SnO2 Structure. *J. Am. Chem. Soc.* **2017**, *139*, 4290−4293.

https://dx.doi.org/10.1021/acsami.0c00412
ACS Appl. Mater. Interfaces 2020, 12, 22760−22770